PSRFlow: Probabilistic Super Resolution with Flow-Based Models for Scientific Data

Jingyi Shen (iD) and Han-Wei Shen (iD)

Abstract— Although many deep-learning-based super-resolution approaches have been proposed in recent years, because no ground truth is available in the inference stage, few can quantify the errors and uncertainties of the super-resolved results. For scientific visualization applications, however, conveying uncertainties of the results to scientists is crucial to avoid generating misleading or incorrect information. In this paper, we propose PSRFlow, a novel normalizing flow-based generative model for scientific data super-resolution that incorporates uncertainty quantification into the super-resolution process. PSRFlow learns the conditional distribution of the high-resolution data based on the low-resolution counterpart. By sampling from a Gaussian latent space that captures the missing information in the high-resolution data, one can generate different plausible super-resolution outputs. The efficient sampling in the Gaussian latent space allows our model to perform uncertainty quantification for the super-resolved results. During model training, we augment the training data with samples across various scales to make the model adaptable to data of different scales, achieving flexible super-resolution for a given input. Our results demonstrate superior performance and robust uncertainty quantification compared with existing methods such as interpolation and GAN-based super-resolution networks.

Index Terms—Super resolution, latent space, normalizing flow, uncertainty visualization

---

◆

---

1 INTRODUCTION

The ability to conduct high-resolution simulations is crucial for obtaining a deep understanding of scientific phenomena. When data are stored at a lower resolution due to I/O and storage constraints, the resulting low-quality visualization suffers from information loss, which makes scientific discovery more difficult. Recently, many deep learning-based methods have been proposed for scientific data super-resolution. These methods learn the complex correspondence between low and high-resolution data, and have shown remarkable performance. [2, 13–16, 39–41]

Although widely used, several limitations still remain for deep learning-based super-resolution methods. First, current methods learn a deterministic one-to-one mapping between high and low-resolution data pairs. During inference, given a low-resolution input, the model predicts one single high-resolution output. However, due to the loss of information in the low-resolution data, it is not possible to precisely determine the exact high-resolution output given the input, because one low-resolution data may correspond to multiple high-resolution outputs. Existing methods do not directly tackle the challenge of modeling such variations in the super-resolution process. Another challenge of the existing learning-based super-resolution methods is that in the inference stage, since no high-resolution ground truth is available, quantifying the errors and uncertainties of the super-resolved result is difficult. However, to avoid making wrong decisions based on the super-resolved data, it is crucial to convey uncertainties and provide indications about the quality of the super-resolution outputs to scientists. Currently, there is relatively little research on modeling the uncertainties associated with neural network-based super-resolution outputs.

In this paper, we propose PSRFlow, a novel probabilistic super-resolution approach based on the invertible normalizing flow [10,24,32]. Normalizing flows are constructed based on a sequence of invertible transformations that convert a simple distribution into a more complex one. By using a conditional normalizing flow to model the distribution of high-resolution data conditioned on low-resolution inputs, we can overcome the limitations of existing techniques. First, rather than mod-

eling a deterministic one-to-one mapping, we treat super-resolution as a conditional generation process. We model the prior knowledge of missing high-frequency information as a Gaussian distribution in the latent space conditioned on the low-resolution data. We choose Gaussian distributions since they are easy to work with and efficient to sample. Once the conditional distribution is well-learned, we can sample a latent vector from the distribution and reconstruct plausible high-resolution data. Second, we utilize normalizing flows to capture the complex relationship between low and high-resolution data. By modeling the missing information of high-resolution data as simpler Gaussian distributions in the latent space, PSRFlow can explicitly capture the variations among the high-resolution data for a given low-resolution input. Samples drawn from the Gaussian latent space reflect the uncertainties in the high-resolution data generation process. Regions with higher variations indicate that the model is less confident in those areas and thus errors are more likely to occur. As a result, the reliability of PSRFlow is boosted, since even without the ground truth it is still possible to convey potential errors to scientists during inference.

Our PSRFlow is an invertible framework that effectively captures the relationships between low and high-resolution data. The forward process of PSRFlow gradually transforms the high-resolution data in the original complex data space to a latent space with two components. One latent subspace encodes low-resolution information, while the other latent subspace follows a Gaussian distribution and captures the missing high-frequency information conditioned on the low-resolution information. In the reverse process of PSRFlow, missing high-frequency information can be estimated by sampling from the Gaussian latent space. By combining this information with the low-resolution latent vector extracted by an encoder, and leveraging the invertible transformations of normalizing flow, PSRFlow can produce a high-quality super-resolution output. When sampling the Gaussian latent space multiple times, scientists can estimate the uncertainties of the super-resolution results by computing the variations of the super-resolved outputs at each voxel. In addition, during training, we augment the training data with samples from various scales so that once PSRFlow is trained, it can be adaptively applicable for super-resolution across different scales, allowing us to achieve flexible super-resolution for a given low-resolution input with one trained model.

Based on the learned distribution mappings, given low-resolution data, scientists can obtain different plausible super-resolved results by sampling the Gaussian latent space. In contrast to other super-resolution methods in the visualization literature, our method allows exploring the super-resolved data space and estimating the uncertainties of the super-resolution results. The results of our qualitative and quantitative evaluations demonstrate that our super-resolution method has superior

---

- *Jingyi Shen and Han-Wei Shen are with the Department of Computer Science and Engineering, The Ohio State University. E-mail: {shen.1250 and shen.94}@osu.edu.*

performance with robust uncertainty quantification, compared to existing interpolation and generative adversarial network (GAN) based super-resolution methods. The contributions of our work are threefold:

- First, we propose a novel probabilistic super-resolution approach based on normalizing flow to model the missing information of high-resolution data as distributions instead of a deterministic one-to-one mapping as in the existing learning-based methods.
- Second, our method provides uncertainty quantification to increase the reliability of the model for scientists to make informed decisions.
- Third, with data augmentation and cross-scale training, we allow flexible super-resolution for data from different resolution levels with one trained model.

2 RELATED WORKS

We adopt invertible normalizing flow for probabilistic super-resolution with uncertainty estimation. In this section, we summarize the related works of scientific data super-resolution, uncertainty analysis of scientific data, and the applications of normalizing flow.

Scientific Super-Resolution for Visualization. Many deep-learning-based super-resolution approaches have been proposed for scientific data. SSR-TVD [15] utilizes a generative adversarial network (GAN) for spatial super-resolution of time-varying data with temporal coherence. SSR-VFD [13] upscales the low-resolution vector field spatially. Weiss et al. [39] upscale low-resolution isosurfaces to high-resolution with ambient occlusion to reduce full-resolution rendering time. Instead of uniform grid super-resolution, Wurster et al. [13] utilize a hierarchy of super-resolution models for upscaling data with varying levels of detail. For temporal super-resolution, TSR-TVD [14] generates missing time steps in time-varying data from a low temporal resolution volume sequence. STSRNet [2] introduces a two-stage framework (upscale temporal dimension first then spatial) for spatial-temporal super-resolution of time-varying vector fields given low-resolution key time steps as input. STNet [16] utilizes feature-space temporal interpolation and feature upscaling to synthesize spatiotemporal super-resolution volumes for time-varying data. TempoGAN [41] utilizes a novel temporal discriminator to produce highly detailed and temporally coherent four-dimensional fields for fluid flows. However, no existing work has investigated the uncertainties introduced in the super-resolution process. For scientific visualization and analysis, conveying uncertainties is crucial for scientists to avoid making misleading or incorrect decisions. To fill this gap, in this paper, we propose probabilistic super-resolution with uncertainty quantification for scientific visualization.

Normalizing Flow Applications. Our work is based on one of the powerful generative models named normalizing flow [10, 24, 32]. Due to its ease of training and fast inference, normalizing flow has been used for various tasks such as image super-resolution [21, 22, 25, 27], point cloud generation [29, 42], and speech synthesis [1], etc. Our work leverages the theory presented in Ardizzone et al. [3], which approximates a conditional distribution through a tractable distribution where an extra latent variable is introduced to mitigate the information loss. In our case, the lost information is the high-frequency details that get smoothed out during downsampling which can be captured by the Gaussian latent variable.

Uncertainty Visualization. Uncertainty visualization has become a top visualization research direction to avoid generating misleading interpretations of data. Uncertainties can be introduced in different stages of visualization pipeline, including data acquisition [5, 7, 30, 31, 36], data transformation [9, 19, 34], visual mapping and rendering [6, 11, 12, 26, 28, 33] stages. In deep learning for scientific visualization, Han et al. [17] found that the model's performance is affected by flow behavior. Regions with greater separation in the flow field have higher errors. Our work focuses on the uncertainty in the data transformation stage, where low-resolution data are super-resolved into high-resolution counterparts.

3 BACKGROUND: NORMALIZING FLOW MODEL

Our work is based on a conditional normalizing flow to model the complex relationship between low and high-resolution data for scientific super-resolution with uncertainty estimation. In this section, we briefly introduce the normalizing flow model.

Normalizing flows is a type of generative neural network used to model complex probability distributions. It learns a bijective mapping between the data space with a complex distribution and a latent space with a simple base distribution (typically a Gaussian distribution) through a sequence of simple and invertible mappings (i.e., "flows"). By learning such bijective mappings, one can model the complex probability density of data and sample from the simple latent distribution to produce in-distribution complex data samples.

As shown in Fig. 1, if we denote the invertible mapping as f, the ***forward direction*** (or ***generation direction***) of f is to gradually transform a variable Z with a known and tractable probability density $p(Z)$ into a random variable X with complex probability density $p(X)$, denoted as $X = f(Z)$. Note that one can generate a sample $\mathbf{x}$ by sampling $\mathbf{z}$ from the base distribution $p(Z)$ and applying the forward transformation $\mathbf{x} = f(\mathbf{z})$. Due to the invertibility of f, the ***backward direction*** (or ***normalizing direction***) of f is to transform from complex data distribution into simple latent distribution: $Z = f^{-1}(X)$.
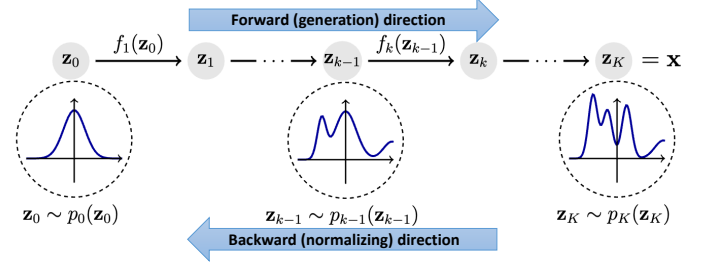

Fig. 1: Normalizing flow distribution transformation [20]. The forward direction transforms a simple distribution into a complex one step by step. This process is invertible in the backward direction.

Generally, the invertible function f is composed of K invertible and learnable transformations: $f = f_1 \circ f_2 \circ \cdots \circ f_K$. So we have:

$$\mathbf{x} = \mathbf{z}_K = f_K \circ f_{K-1} \circ \cdots \circ f_1(\mathbf{z}_0) \tag{1}$$

where $\mathbf{z}_0$ has a probability density $p_0(\mathbf{z}_0)$, which is the base distribution (e.g. a standard normal distribution). Each f_k is an invertible and differentiable transformation. The probability density of $\mathbf{x}$ is computed by repeatedly applying the change-of-variable formula, and since the determinant of products equals the product of determinants, we have:

$$p(\mathbf{x}) = p_K(\mathbf{z}_K) = p_0(\mathbf{z}_0) \prod_{k=1}^{K} \left| \det \frac{\partial f_k(\mathbf{z}_{k-1})}{\partial \mathbf{z}_{k-1}} \right|^{-1} \tag{2}$$

Taking logarithm of Eq. (2), we have:

$$\log p(\mathbf{x}) = \log p_K(\mathbf{z}_K) = \log p_0(\mathbf{z}_0) - \sum_{k=1}^{K} \log \left| \det \frac{\partial f_k(\mathbf{z}_{k-1})}{\partial \mathbf{z}_{k-1}} \right| \tag{3}$$

In Eq. (3), the first term on the right is the log probability density of the latent distribution, and the second term is the volume change caused by the transformation. It has been formally proven that if the transformation function f can be arbitrarily complex, one can generate any target distribution with any latent distribution [8]. Function f is parameterized by θ and is learnable. The optimization goal for normalizing flows is to find θ that maximizes the log-likelihood, which is equal to $\log p(\mathbf{x})$ and can be directly computed using Eq. (3). One way to interpret this is from the statistical distance perspective, where maximizing log-likelihood is equivalent to minimizing the KL divergence between true data distribution and the flow-parameterized data distribution.

Constructing invertible transformations can be difficult since it requires invertibility of each f_k and easy-to-compute Jacobian determinant $det(J_{f_k})$ in Eq. (3). One common approach is utilizing the invertible "affine coupling layer" [10] whose determinant can be efficiently computed as the product of diagonal elements of the Jacobian matrix. As shown in Fig. 2 (left), the affine coupling layer partitions the input $\mathbf{z}$ of this layer into two subspaces ($\mathbf{z}_{1:d}$ and $\mathbf{z}_{d+1:D}$) and applies a differentiable affine transformation to $\mathbf{z}_{d+1:D}$ while keeping $\mathbf{z}_{1:d}$

untouched. d is the splitting dimension. The scale and shift parameters for affine transformation are computed based on the untouched $\mathbf{z}_{1:d}$. Formally, the affine coupling layer's output $\mathbf{z}'$ can be computed by:

$$\mathbf{z}'_{1:d} = \mathbf{z}_{1:d}$$
$$\mathbf{z}'_{d+1:D} = \mathbf{z}_{d+1:D} \odot \exp(S(\mathbf{z}_{1:d})) + T(\mathbf{z}_{1:d}) \tag{4}$$

$\odot$ denotes the element-wise Hadamard product. Functions $S(\cdot)$ and $T(\cdot)$ can be highly complex (e.g., neural networks) and non-invertible. They take $\mathbf{z}_{1:d}$ as input and predict scale and translation parameters to apply on $\mathbf{z}_{d+1:D}$. The high modeling capability of $S(\cdot)$ and $T(\cdot)$ is the key to the effectiveness of coupling layers. The inverse of Eq. (4) is:

$$\mathbf{z}_{1:d} = \mathbf{z}'_{1:d}$$
$$\mathbf{z}_{d+1:D} = (\mathbf{z}'_{d+1:D} - T(\mathbf{z}'_{1:d})) \odot \exp(-S(\mathbf{z}'_{1:d})) \tag{5}$$
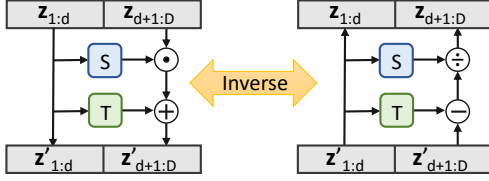

Fig. 2: The computation graph of an affine coupling layer in the forward (left) and its inverse (right) direction.

Note that one subspace of the variable (i.e., $\mathbf{z}_{1:d}$) remains identical after transformation, which reduces the modeling ability of the normalizing flow. To solve this, channel order permutation [10, 24] is usually adopted to make sure all variable dimensions got transformed. Besides this, normalizing flows often contain invertible activation normalization layers (i.e., "actnorm") [24] to normalize feature maps for stable gradients and faster convergence. By stacking multiple invertible coupling layers along with normalization and permutation (known as flow steps), normalizing flows can scale and shift input variables multiple times and learn complex dependencies between variables, making it possible to transform between complex and simple distributions.

As a generative model, normalizing flows do not have mode collapse and training instability issues like generative adversarial networks (GANs) or Variational Autoencoders (VAEs) [4]. Meanwhile, normalizing flows allow exact log-likelihood evaluation and efficient latent space sampling. With this, we can use normalizing flows to model complex distribution mappings between low and high-resolution data. In the next section, we will present our uncertainty-aware super-resolution method for scientific data based on a conditional normalizing flow.

4 METHOD

Super-resolution is a challenging problem due to the inherent difficulties in recovering missing information. In our paper, instead of learning a deterministic one-to-one mapping between low and high-resolution data, we propose PSRFlow, which takes a probabilistic approach to model the conditional distribution of missing information in high-resolution data given the low-resolution input. Our approach not only allows high-quality super-resolution but also provides uncertainty estimation of the results, which is particularly important for scientists to make reliable decisions about the underlying scientific phenomenon.

4.1 Overview

Given the low-resolution data $Y \in \mathbb{R}^{D \times H \times W}$, we aim to generate its super-resolved counterpart $X \in \mathbb{R}^{rD \times rH \times rW}$, where r is the upscaling factor. Figure 3 shows the overview of PSRFlow. The motivation for using the normalizing flow model for our task is threefold. First, instead of a deterministic one-to-one mapping, normalizing flow allows explicit and efficient probabilistic modeling of the relationship between high and low-resolution data. Second, compared to other generative models like GANs and VAEs, normalizing flows are more stable. Third, straightforward latent space sampling of normalizing flow allows uncertainty quantification of the super-revolved outputs. PSRFlow utilizes a conditional normalizing flow (CNF) to convert high-resolution data into a latent space consisting of two parts. One part contains low-resolution information, while the other is a Gaussian latent space that encodes the
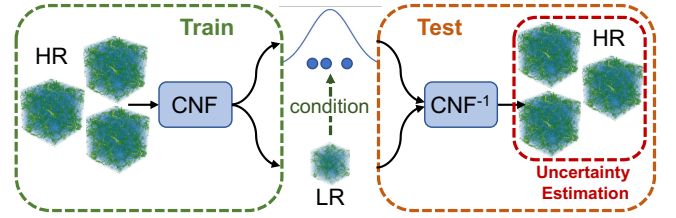

Fig. 3: Overview of PSRFlow. High-frequency details and low-resolution (LR) information are modeled separately in the latent space through a conditional normalizing flow (CNF). The high-frequency latent follows a distribution conditioned on LR. During testing, given LR input, one can sample from the conditional distribution and utilize the inverse of CNF to obtain HR outputs. HR outputs are then used for uncertainty estimation.

missing high-frequency information conditioned on the low-resolution data. The reason for transforming data into a latent space with Gaussian distribution is that Gaussian space is easier to control and sample. During inference, one can sample from the Gaussian latent space for high-frequency information reconstruction. By combining the sampled high-frequency details with the low-resolution information and utilizing the inverse transformation of the conditional normalizing flow (CNF^{-1}), we can obtain a possible high-resolution output.

4.2 Conditional Normalizing Flow for Super Resolution

The general procedure of super-resolution is to recover high-resolution data X by predicting the missing high-frequency details of a given low-resolution data Y. While existing super-resolution approaches learn a deterministic mapping $Y \to X$, we focus on modeling the conditional distribution $P(X \mid Y)$. In this section, we discuss: (1) how to capture the complex relationship between low and high-resolution data, and (2) how to model the missing high-frequency information.

4.2.1 High-Resolution Conditional Modeling

Modeling distribution $P(X \mid Y)$ is more challenging than predicting one high-resolution output, as additional effort is required to capture the complex information such as how the data is placed in high-dimensional space. To solve this, we propose a data-driven approach by utilizing an invertible conditional normalizing flow to parameterize and learn such conditional distribution.

Inspired by Fourier domain signal processing, one can decompose data into high and low-frequency components. Given a smooth low-resolution input, it is possible to get a high-resolution output by adding high-frequency details into the low-resolution data. With this, based on the probability chain rule, the conditional distribution $P(X \mid Y)$ can be further explained into:

$$P(X \mid Y) = P(X_h, X_l \mid Y) = P(X_h \mid X_l, Y)P(X_l \mid Y) \tag{6}$$

where X_h and X_l are the high and low-frequency components, respectively. $P(X_h \mid X_l, Y)$ means instead of random noise, we consider the missing high-frequency details to be conditioned on the low-resolution information. However, modeling distribution in the original data space is non-trivial due to the intractable probability density. This motivates us to utilize conditional normalizing flow since it learns to transform data with complicated and intractable probability density $P(X|Y)$ into a simpler latent space with tractable probability density $P(Z|Y)$. If the model is well-trained, we can derive $P(X|Y)$ explicitly from $P(Z|Y)$ via Eq. (2). Transforming data into the latent space can also facilitate information decomposition of the high-resolution data.

As shown in Fig. 4, given a pair of high-resolution $\mathbf{x} \in X$ and low-resolution data $\mathbf{y} \in Y$, we first transform $\mathbf{x}$ through a sequence of normalizing flow steps into a latent representation $\mathbf{z}$. Then, we decompose $\mathbf{z}$ into two components, namely $\mathbf{z}_h$ and $\mathbf{z}_l$, where we force $\mathbf{z}_h$ to capture high-frequency details and $\mathbf{z}_l$ to capture the low-frequency information based on the low-resolution data $\mathbf{y}$. We formulate this process as:

$$g(\mathbf{x}) = \mathbf{z}, \quad \text{where } \mathbf{z} = (\mathbf{z}_h, \mathbf{z}_l) \tag{7}$$
$$p(\mathbf{z}_h, \mathbf{z}_l \mid \mathbf{y}) = p(\mathbf{z}_h \mid \mathbf{z}_l, \mathbf{y})p(\mathbf{z}_l \mid \mathbf{y}) \tag{8}$$

where g is the invertible normalizing flow and (,) means $\mathbf{z}$ is decomposed into $\mathbf{z}_h$ and $\mathbf{z}_l$. The decomposition in PSRFlow is implemented

by latent space channel splitting. This splitting can be interpreted as projecting information onto two subspaces of the latent space. The inverse of g is the generative direction: $g^{-1}((\mathbf{z}_h, \mathbf{z}_l)) = \mathbf{x}$. Equation (8) is the key and goal for our probabilistic super-resolution. The only difference to Eq. (6) is that this is modeled in the latent space but will be transformed back to the data space with the help of flow g.
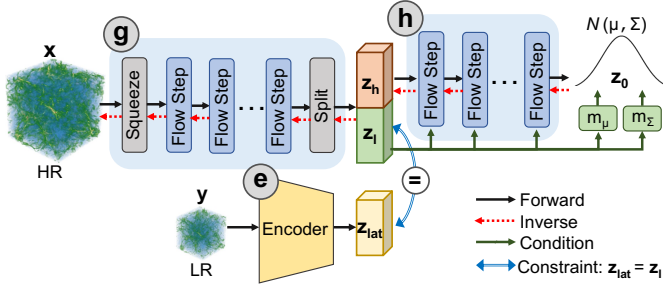

Fig. 4: Architecture of PSRFlow. During training, input high-resolution $\mathbf{x}$ is transformed into a latent space with two components: $\mathbf{z}_h$ (high-frequency information) and $\mathbf{z}_l$ (low-resolution information) by flow g. Encoder e is used to facilitate information decomposition so that $\mathbf{z}_l$ matches the target low-resolution latent representation $\mathbf{z}_{lat}$ extracted by e. $\mathbf{z}_h$ is further transformed by conditional flow h into $\mathbf{z}_0$ with a Gaussian distribution. During inference, encoder e and the inverse of g and h (red dashed arrow) are used to recover a high-resolution output.

The challenge now is how to enforce $\mathbf{z}_h$ and $\mathbf{z}_l$ to capture the desired information. In many normalizing flow applications [3, 42], input data is transformed into a standard Gaussian distribution in the latent space, i.e., $\mathbf{z} \sim \mathcal{N}(0, I)$. However, scientific data often have complex features across different regions and time steps, and representing such complicated information using a standard Gaussian distribution may not be feasible. Thus, we impose a constraint on $\mathbf{z}_l$ to enforce it to encode low-resolution information, whereas we further transform $\mathbf{z}_h$ into a Gaussian latent space that captures the missing information between low and high-resolution data. Instead of standard Gaussian distributions, the parameters of this Gaussian latent space are predicted based on the low-resolution data.

4.2.2 Low-Resolution Encoding

To ensure that $\mathbf{z}_l$ encodes the low-resolution information, in Fig. 4, PSRFlow has another low-resolution encoding network e to add explicit supervision to $\mathbf{z}_l$. Encoder e does not need to be invertible, and is built based on the popular ResNet (Residual Network) [18] to progressively extract a low-resolution representation $\mathbf{z}_{lat}$ from low-resolution data $\mathbf{y}$:

$$\mathbf{z}_{lat} = e(\mathbf{y}) \tag{9}$$

During training, $\mathbf{z}_l$ is constrained to match $\mathbf{z}_{lat}$. During inference, with the well-trained encoder e, given a low-resolution data $\mathbf{y}$, we can replace $\mathbf{z}_l$ with encoder generated $\mathbf{z}_{lat}$ without hurting the reconstruction quality of normalizing flow g. This is ensured by the invertibility of flow g. So we have $g^{-1}((\mathbf{z}_h, \mathbf{z}_l)) = g^{-1}((\mathbf{z}_h, \mathbf{z}_{lat})) = \mathbf{x}$. Due to the deterministic mapping in Eq. (9) and since $\mathbf{z}_l$ is forced to match $\mathbf{z}_{lat}$, we have $p(\mathbf{z}_{lat} \mid \mathbf{y}) = p(\mathbf{z}_l \mid \mathbf{y}) = 1$. We reformulate Eq. (8) into:

$$p(\mathbf{z}_h, \mathbf{z}_l \mid \mathbf{y}) = p(\mathbf{z}_h \mid \mathbf{z}_l, \mathbf{y}) = p(\mathbf{z}_h \mid \mathbf{y}) \tag{10}$$

Equation (10) indicates that instead of treating the decomposed high-frequency information as independent noise, we consider it to be dependent on the low-resolution data.

4.2.3 High-Frequency Modeling

To fully capture the complex variations of high-frequency details given the low-resolution data, i.e., $p(\mathbf{z}_h \mid \mathbf{y})$, in Fig. 4, we further transform $\mathbf{z}_h$ through a conditional normalizing flow h into a simpler Gaussian latent space $\mathbf{z}_0$ with predicted mean μ and variance Σ. Different from previous layers in unconditional flow g, flow steps in h take an additional input $\mathbf{z}_l$ as a condition when transforming its input $\mathbf{z}_h$ into the innermost latent space $\mathbf{z}_0$, as shown in Fig. 4 (green arrow). The condition $\mathbf{z}_l$ is used as additional information for scaling and transformation parameter

prediction of affine coupling layers in flow h. More details about affine coupling layers can be found in Sec. 3. Thus, we have:

$$h(\mathbf{z}_h, \mathbf{z}_l) = \mathbf{z}_0 \tag{11}$$

$$p(\mathbf{z}_0 \mid \mathbf{y}) = \mathcal{N}(\mu, \Sigma), \quad \text{where } \mu = m_\mu(\mathbf{y}) \text{ and } \Sigma = m_\Sigma(\mathbf{y}) \tag{12}$$

where m_μ and m_Σ are Gaussian distribution prediction networks for the missing information. Due to the invertibility of flow h, we can derive $p(\mathbf{z}_h \mid \mathbf{y})$ from Gaussian distribution $p(\mathbf{z}_0 \mid \mathbf{y})$. Further, based on the invertibility of flow g, we can derive $p(\mathbf{x} \mid \mathbf{y})$ from $p(\mathbf{z}_h, \mathbf{z}_l \mid \mathbf{y})$.

4.3 Uncertainty Quantification

Uncertainty quantification is crucial for scientific visualization and analysis of super-resolved data since it will provide scientists with indications about the quality of results. In this section, we discuss how to estimate uncertainties of PSRFlow's high-resolution outputs.

4.3.1 Conditional Distribution Modeling

It is intractable to compute the conditional distribution of high-resolution data $\mathbf{x}$ given low-resolution data $\mathbf{y}$ in the original data space. As discussed in the previous section, we parameterize such conditional distribution through the proposed PSRFlow. According to Eq. (2), Eq. (10) and Eq. (12), exact conditional distribution $p(\mathbf{x} \mid \mathbf{y})$ can be explicitly computed via the generation direction of flow as:

$$p(\mathbf{x} \mid \mathbf{y}) = p(\mathbf{z}_h \mid \mathbf{y}) \prod_{k=1}^{K_g} \left| \det \frac{\partial g_k^{-1}(\mathbf{z}_{k-1})}{\partial \mathbf{z}_{k-1}} \right|^{-1},$$

$$\text{where } p(\mathbf{z}_h \mid \mathbf{y}) = p(\mathbf{z}_0 \mid \mathbf{y}) \prod_{k=1}^{K_h} \left| \det \frac{\partial h_k^{-1}(\mathbf{z}_{k-1})}{\partial \mathbf{z}_{k-1}} \right|^{-1} \tag{13}$$

$$\text{and } p(\mathbf{z}_0 \mid \mathbf{y}) = \frac{1}{\sqrt{(2\pi)^D |\Sigma|}} \exp\left(-\frac{1}{2} (\mathbf{z}_0 - \mu)^\top \Sigma^{-1} (\mathbf{z}_0 - \mu) \right)$$

where $\mathbf{z}_h$ is the high-frequency latent component and D is the dimensionality of the Gaussian latent $\mathbf{z}_0$. K_g and K_h are the total number of invertible flow steps in g and h, respectively. g_k^{-1} is inverse of the k-th layer in flow g and $\mathbf{z}_{k-1}$ is the input of this inverse function.

As discussed in Sec. 3, maximizing the conditional log-likelihood $\log p(\mathbf{x} \mid \mathbf{y})$ is equal to minimizing the KL divergence between the true conditional data distribution and the flow parameterized data distribution. Thus, we incorporate $\log p(\mathbf{x} \mid \mathbf{y})$ into our training loss in Sec. 4.4. Once the model is well-trained, high-frequency details will be captured in the Gaussian latent space $\mathbf{z}_0$. One advantage of PSRFlow is that it allows accurate and efficient posterior sampling of high-resolution data by sampling from this Gaussian latent space.

4.3.2 Uncertainty Aware Super-Resolution

With explicit conditional distribution modeling, we can efficiently sample the Gaussian latent space for high-quality high-resolution data reconstruction. Moreover, these samples reflect the uncertainty in the high-resolution data generation process. In this section, we discuss how to quantify uncertainties in the super-resolution process.

During inference, to produce one high-resolution output, as shown in Algorithm 1, PSRFlow first extracts the low-resolution latent representation $\mathbf{z}_{lat}$ from the low-resolution input $\mathbf{y}$ using encoder e. Due to the constraint that we added during training, $\mathbf{z}_{lat}$ can replace $\mathbf{z}_l$ without hurting the representation quality. Then, PSRFlow utilizes $\mathbf{z}_l$ (equal to $\mathbf{z}_{lat}$) to predict mean (μ) and variance(Σ) of the innermost Gaussian latent space $\mathbf{z}_0$. This latent space captures the variations of the missing high-frequency details and by sampling from it and utilizing the inverse of flow h, PSRFlow can recover a plausible missing high-frequency information $\mathbf{z}_h$. PSRFlow then concatenates $\mathbf{z}_h$ and $\mathbf{z}_l$, and apply the inverse of flow g to obtain one possible high-resolution output. By sampling the Gaussian latent space and repeating this process by N times, let $\mathbf{x}'^{(i)}$ denote the i-th generated high-resolution output, we can compute the mean $\bar{\mathbf{x}}$ and standard deviation $\mathbf{x}_\sigma$ of high-resolution outputs using Algorithm 1. The mean $\bar{\mathbf{x}}$ is used as the super-resolution final output and the standard deviation $\mathbf{x}_\sigma$, which measures the variations in the high-resolution data, is served as an estimation of the uncertainty.

Our architecture is specifically designed for a $2\times$ upscaling factor in all three dimensions of the volumetric data (increase data size by a factor of $8\times$). With data augmentation and cross-scale training, as discussed in Sec. 4.5.2, we allow flexible super-resolution by recursively applying our trained model with a $2\times$ upscaling factor for each iteration.

Algorithm 1: Uncertainty Aware Super-resolution

Input : A low-resolution data $\mathbf{y}$
Output : A super-resolved data $\bar{\mathbf{x}}$ and uncertainty estimation $\mathbf{x}_\sigma$
$\mathbf{z}_{lat} = e(\mathbf{y})$
$\mathbf{z}_l = \mathbf{z}_{lat}$
$\mu = m_\mu(\mathbf{z}_l)\,, \Sigma = m_\Sigma(\mathbf{z}_l)$
/* Sample Gaussian latent space $\mathbf{z}_0$ N times, and
   estimate mean $\bar{\mathbf{x}}$ and variance $\mathbf{x}_\sigma$ of
   high-resolution outputs.   */
for $i \leftarrow 1$ **to** N **do**
$\quad \mathbf{z}_0^{(i)} \sim \mathcal{N}(\mu, \Sigma)$
$\quad \mathbf{z}_h^{(i)} = h^{-1}(\mathbf{z}_0^{(i)}, \mathbf{z}_l)$
$\quad \mathbf{x}'^{(i)} = g^{-1}([\mathbf{z}_h^{(i)}, \mathbf{z}_l])$ // $\mathbf{x}'^{(i)}$ is a high-res output
$\quad X.append(\mathbf{x}'^{(i)})$
$\bar{\mathbf{x}} = \frac{1}{N}\sum_{i=1}^{N} X(i)$
$\mathbf{x}_\sigma = \sqrt{\frac{1}{N}\sum_{i=1}^{N}(X(i) - \bar{\mathbf{x}})^2}$
return $\bar{\mathbf{x}}, \mathbf{x}_\sigma$

4.3.3 Uncertainty Visualization

To analyze uncertainties in the super-resolution results, we utilize three uncertainty visualization methods. The first method directly visualizes the estimated variation field ($\mathbf{x}_\sigma$). The second approach encodes output variations ($\mathbf{x}_\sigma$) on the isosurfaces using color. The third method is based on the Probabilistic Marching Cubes algorithm proposed by Pöthkow et al. [31]. For each low-resolution input, N possible high-resolution outputs are generated using Algorithm 1. The mean and covariance matrix for each voxel of the generated high-resolution outputs are computed. The level-crossing probability is calculated by randomly sampling n instances from the computed multivariate Gaussian distribution and applying the level-crossing criteria. The probability is computed as m/n where m is the number of samples that pass through the voxel [31].

4.4 Loss Functions

We formulate the super-resolution problem as the conditional generation of high-resolution data based on low-resolution data utilizing a normalizing flow model f_θ parameterize by θ. Note that f_θ is the combination of flow g and h in our approach. The optimal parameter θ can be found in a data-driven manner by feeding the network with M high and low-resolution training data pairs $\{(\mathbf{x}^{(i)}, \mathbf{y}^{(i)})\}_{i=1}^{M}$. By maximizing the log-likelihood of high-resolution $\mathbf{x}$ conditioned on low-resolution $\mathbf{y}$, i.e., $\log p(\mathbf{x} \mid \mathbf{y})$, the model learns the data generation process. So the first loss we want to minimize is the negative log-likelihood loss $\mathscr{L}_{sr}$:

$$\mathscr{L}_{sr} = \mathbb{E}_{\mathbf{x},\mathbf{y}}[-\log p(\mathbf{x} \mid \mathbf{y})] \tag{14}$$

To ensure that one component of the normalizing flow's latent space (i.e., $\mathbf{z}_l$) encodes the low-resolution information, the second loss we want to minimize is the L1 loss between flow g's latent representation $\mathbf{z}_l$ and low-resolution encoder e's output $\mathbf{z}_{lat}$:

$$\mathscr{L}_{lat} = \mathbb{E}_{\mathbf{x},\mathbf{y}}[\|\mathbf{z}_{lat} - \mathbf{z}_l\|_1] \tag{15}$$

where $\mathbf{z}_l$ and $\mathbf{z}_{lat}$ can be computed from Eq. (7) and Eq. (9), respectively. In our work, normalizing flow models (g and h) and the encoder e in PSRFlow are trained together through a combination of these two losses. We formulate our total training loss as:

$$\mathscr{L} = \mathscr{L}_{sr} + \lambda \mathscr{L}_{lat} \tag{16}$$

Our optimization goal is to minimize loss $\mathscr{L}$. Since high-resolution reconstruction and low-resolution encoding have different learning difficulties, a hyperparameter λ is used in our loss to balance their

optimization. The first loss $\mathscr{L}_{sr}$ is used to optimize the parameters of flow g and h so that the data is successfully transformed into a predicted Gaussian latent space. Concurrently, the second loss $\mathscr{L}_{lat}$ is used to constrain $\mathbf{z}_l$ and optimize flow g to minimize the difference between $\mathbf{z}_l$ and $\mathbf{z}_{lat}$. Meanwhile, $\mathscr{L}_{lat}$ will also optimize parameters of encoder e to make $\mathbf{z}_{lat}$ more similar to $\mathbf{z}_l$. Although it may introduce a moving-target problem, these two losses in PSRFlow are not competing with each other like GANs. Instead, one loss constrains the optimization of the other so that the models are still consistently optimized to reduce both $\mathscr{L}_{sr}$ and $\mathscr{L}_{lat}$.

4.5 Implementation

4.5.1 Flow Architecture

The invertibility for probability computation of normalizing flow is assured by design. The invertible flow g and h are based on the widely used Glow model [24] which consists of several stacked flow steps. These flow steps are the key to the invertibility and the modeling capacity of the normalizing flow. By stacking multiple flow steps as shown in Fig. 4, the model has the ability to learn the transformations between the Gaussian latent space and the high-resolution data space.

4.5.2 Block-based Processing and Cross Scale Training

We train and evaluate our model based on data blocks from multiple scales. During training, the raw data is downscaled by a factor of 2^n and 2^{n+1} ($n \geq 0$), and we sample pairs of high-resolution (with scale factor 2^n) and the corresponding low-resolution blocks (with scale factor 2^{n+1}) for training. The model is trained to learn upscaling the input of different resolutions by a factor of $2\times$. This training strategy improves the model's ability and robustness to be applicable to a range of scales. During inference, since our model is entirely based on convolutional layers, we can utilize one trained model recursively across multiple scales for flexible super-resolution, with each iteration upscaling the data by a scale factor of $2\times$.

To reduce artifacts and errors at block boundaries, we extend each block with extra padding before feeding it into the network. We crop the reconstructed blocks and only keep the central regions for the final output. This also helps reduce the modeling complexity so that instead of learning and sampling from a high-dimensional Gaussian latent space for the entire domain, we focus on modeling the missing information in each local block using a smaller Gaussian latent space.

5 RESULTS

In this section, we evaluate PSRFlow for scientific data super-resolution both quantitatively and qualitatively, and compare it with three baseline methods. Moreover, we demonstrate PSRFlow's superiority in terms of uncertainty quantification, a feature missing from the baseline methods.

Table 1: Dataset name, training data, validation data, the total number of data pairs for training, and high-resolution output block size.

Dataset	Train	Validation	# Training	Block Size
Vortex	ts05, ts10, ts12, ts17, ts20	ts08	1500	16
Nyx	id35, id66 and id88	id20	1050	16
Combustion	ts077, ts080, ts121	ts045	1110	30
Plume	ts427, ts432, ts436, ts437	ts420	1600	16

5.1 Dataset and Training Parameters

We evaluated our method using four scientific datasets, listed in Tab. 1. **Vortex** is a simulation of vortex structure. The data resolution is $128\times128\times128$ with 30 time steps. We randomly sampled 1500 pairs of high and low-resolution data blocks from 5 time steps of the vorticity magnitude field for training. **Nyx** is a cosmological simulation produced by Lawrence Berkeley National Laboratory. The log density field with a resolution $256\times256\times256$ was used for evaluation. We randomly sampled 1050 pairs of blocks from 3 ensemble members for training. **Turbulent Combustion** is a combustion simulation produced by Sandia National Laboratories. It is a time-varying multivariate dataset with resolution $480\times720\times120$ across 122 time steps. We use the vorticity magnitude field for experiments, where 1110 pairs of data blocks from 3 time steps are used for training. **Plume** is a solar plume simulation with

resolution $128\times128\times512$. We utilize the velocity magnitude field for experiments. 1600 pairs of high and low-resolution blocks from 4 time steps are used for training. For detailed information about the specific time steps or ensemble members utilized for training and validation, please refer to Tab. 1.

To demonstrate the generalization ability of PSRFlow, we conduct tests on all time steps that were unseen during training and validation for time-varying data and all unseen ensemble members for the ensemble simulation. To compare PSRFlow's performance with the baseline methods and to provide a concise summary of the testing results, we select a representative test time step and an ensemble member to report and visualize the test results. See supplemental material Section 1 for more details. Note that instead of a single scale, training of all datasets uses blocks from multiple scales. Although our method experiments with scalar datasets, it has the potential to be extended to bivariate, multivariate, or vector datasets by increasing the model's channel size.

Our PSRFlow model is implemented using PyTorch[1] and trained on a single NVIDIA Tesla A100 GPU. The Adam optimizer [23] is used for all datasets, and the learning rate is 10^{-4} for all models.

5.2 Baselines

We compare PSRFlow with three baseline methods: trilinear interpolation, ESRGAN [37], and SSR-TVD [15]. Trilinear interpolation, while simplistic, is a frequently used method to scale up data resolution. SSR-TVD and ESRGAN are all state-of-the-art deep learning based super-resolution methods. SSR-TVD is proposed for scientific data super-resolution and ESRGAN is widely adopted for image super-resolution. We found SSR-TVD performs better when trained without the discriminator. Therefore, we use the original SSR-TVD model as well as a modified version without discriminator, denoted as SSR-TVD (w/o D), as our baselines. For ESRGAN, to keep a similar model size to PSRFlow without affecting its performance, we use 10 stacked residual in residual dense blocks (RRDB) [37] as our baseline. To ensure a fair cross-scale comparison, we modify SSR-TVD (w/ and w/o D) and ES-RGAN to perform $2\times$ (in each of the three data dimensions, so a total of $8\times$) upscaling in one forward pass of the model. The output channel size of the last VoxelShuffle [35] layer in the generator of SSR-TVD is changed and only one VoxelShuffle layer is used in ESRGAN for upsampling. All other components of SSR-TVD are kept the same as the original implementation. The model sizes are shown in Tab. 2.

We train SSR-TVD, SSR-TVD (w/o D), and ESRGAN similarly as PSRFlow with the same training data blocks across different scales. These models are constructed to learn the relationship between high and low-resolution blocks regardless of their scale levels.

Table 2: Model size (G: generator, D: discriminator), total training time, and testing time for an upscale factor of $2\times$ for Vortex data.

Method	Size	Train Time	Test Time
SSR-TVD	G: 51.4 MB D: 10.2 MB	23h26m	12s
SSR-TVD (w/o D)	G: 51.4 MB	23h4m	12s
ESRGAN	G: 20.9 MB D: 1.79 MB	23h43m	5s
PSRFlow (our)	NF: 15.7 MB Encoder: 902 KB	23h48m	4s

5.3 Quantitative Evaluation

In this section, we quantitatively compare PSRFlow's super-resolution results with three baseline methods, i.e., trilinear interpolation, SSR-TVD (w/ and w/o D), and ESRGAN.

5.3.1 Evaluation Metrics

For data level evaluation, we adopt peak signal-to-noise ratio (PSNR) to measure the difference between generated high-resolution data and the ground truth. For image level evaluation, we use the structural similarity index measure (SSIM) [38] to evaluate the quality of volume rendering images. Higher PSNR and SSIM means better quality.

5.3.2 Evaluation on Different Upscaling Factors

Instead of a static upscale factor, due to the cross-scale training strategy, we can upscale the low-resolution data multiple times with a $2\times$ scale factor for each iteration. In our experiments, we use upscale factors from $2\times$, $4\times$, to $8\times$. Note that hereafter the upscale factor means the increase in size per dimension, so the actual low-resolution volumetric data size is increased by factors of $8\times$, $64\times$, and $512\times$, respectively.

In Tab. 3, we evaluate the super-resolution results quantitatively in both data level (PSNR) and image level (SSIM) on four datasets. The results demonstrate that except for the SSR-TVD model, all other three deep learning based super-resolution methods outperform the trilinear interpolation for all upscale factors. The low performance of the SSR-TVD may be due to the instability during GAN's training, where the generator and the discriminator compete against each other. Specifically, through the loss plots we recorded during training, we found that the discriminator dominated the training so that it can always distinguish between the generated and the real data. As a result, the generator failed to improve its performance and cannot produce high-quality super-resolution output to fool the discriminator. When we removed the discriminator and only trained the generator, SSR-TVD (w/o D) performed much better compared to the original SSR-TVD model, as shown in the third row (i.e., SSR-TVD (w/o D)) of each dataset in Tab. 3. The quality of the super-resolution results is largely affected by the GAN model's architecture, which poses a large concern for visualization scientists to trust GANs' results. In general, our PSRFlow has quantitatively comparable performance in both data level and image level for all upscale factors compared to SSR-TVD (w/o D) and ESRGAN for all datasets being evaluated. In Tab. 3, the result also shows that for each test data, if we increase the upscale factor from $2\times$, $4\times$ to $8\times$, PSNR and SSIM will drop for all methods. This is due to the inevitable information loss in the low-resolution data, and thus the high-quality super-resolution becomes more challenging and uncertain. But the learning-based methods still demonstrate higher quality compared to the interpolation-based method.

We conducted tests using PSRFlow on all time steps and ensemble members that were not used during training and validation. In Fig. 5, the x-axis in each plot represents time steps or ensemble member IDs, while the y-axis corresponds to the PSNR values. The color encodes different upscaling factors, with blue, green, and yellow representing $2\times$, $4\times$, and $8\times$, respectively. The results show consistently high reconstruction quality with acceptable variations across all time steps for Plume data and all ensemble members for Nyx data. These results demonstrate PSRFlow's robust performance and its ability to generalize when presented with new low-resolution input. Due to the page limit, more testing results are in Section 2 of the supplemental material.
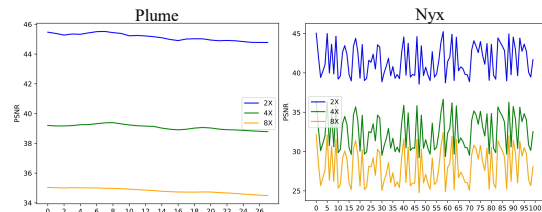

Fig. 5: PSRFlow's test PSNRs for all time steps of Plume data (left) and ensemble members of Nyx data (right).

We compare storage costs and training time of all learning-based super-resolution models, as shown in Tab. 2. The model size of SSR-TVD is 51.4 MB for the generator and 10.2 MB for the discriminator. For ESRGAN, it is 20.9 MB for the generator and 1.79 MB for the discriminator. While our proposed PSRFlow is the most lightweight model with a 15.7 MB normalizing flow model and a 902 KB encoder. Due to the smaller number of parameters, PSRFlow takes less time to train per epoch while a large model such as SSR-TVD is much slower. Besides, PSRFlow evaluates quicker than other large models.

5.4 Qualitative Evaluation

We qualitatively compare the proposed PSRFlow with the baseline methods via volume rendering and isosurface rendering of super-

Table 3: PSNR and volume rendering image SSIM for PSRFlow and baselines' SR output. The best ones within 2% difference are highlighted in bold.

Data	Method	↑PSNR (2×)	↑SSIM (2×)	↑PSNR (4×)	↑SSIM (4×)	↑PSNR (8×)	↑SSIM (8×)
Vortex	Lerp	37.0220	0.9881	27.4537	0.9121	21.6235	0.8218
	SSR-TVD	19.8935	0.8033	16.7406	0.7487	15.4956	0.7336
	SSR-TVD(w/o D)	**47.0051**	**0.9982**	**35.9391**	**0.9759**	**25.1956**	**0.8803**
	ESRGAN	**47.4034**	**0.9988**	**35.6226**	**0.9755**	24.9267	**0.8804**
	PSRFlow (our)	**47.2484**	**0.9980**	**35.5412**	**0.9726**	24.4810	**0.8751**
Nyx	Lerp	35.5707	0.9428	28.5468	0.8224	25.2392	0.7327
	SSR-TVD	22.2846	0.7015	20.5514	0.7495	19.5836	0.7325
	SSR-TVD(w/o D)	38.2107	**0.9835**	30.9282	**0.8984**	26.2338	**0.7521**
	ESRGAN	37.1247	**0.9687**	30.2658	**0.8861**	25.9154	**0.7634**
	PSRFlow (our)	**39.6287**	0.9669	30.4229	0.8616	**26.0397**	**0.7519**
Combustion	Lerp	43.4335	0.9784	34.9869	0.8737	30.4519	0.7557
	SSR-TVD	20.8376	0.3943	17.7482	0.3096	16.0370	0.2944
	SSR-TVD(w/o D)	40.3971	**0.9804**	35.4757	**0.8930**	30.7108	0.7522
	ESRGAN	**48.4751**	**0.9919**	**38.7662**	**0.9310**	**32.0014**	**0.7825**
	PSRFlow (our)	**48.5449**	**0.9927**	37.7999	**0.9232**	31.5086	**0.7892**
Plume	Lerp	**45.9200**	**0.9957**	**38.7633**	**0.9836**	33.3626	0.9596
	SSR-TVD	35.1342	0.9348	30.7222	0.9092	27.6458	0.8929
	SSR-TVD(w/o D)	44.3590	0.9853	36.6536	0.9303	34.0981	0.9153
	ESRGAN	**45.3892**	**0.9924**	**38.8778**	**0.9796**	34.1121	**0.9608**
	PSRFlow (our)	**45.0816**	**0.9952**	**39.2172**	**0.9843**	**35.1595**	**0.9700**

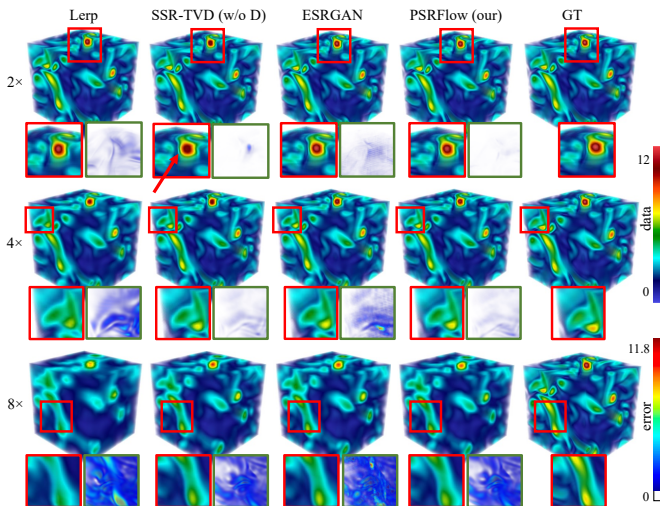Fig. 6: Volume rendering of baselines' and PSRFlow's super-resolution results, error maps (green rectangle), and ground truth for Vortex data.
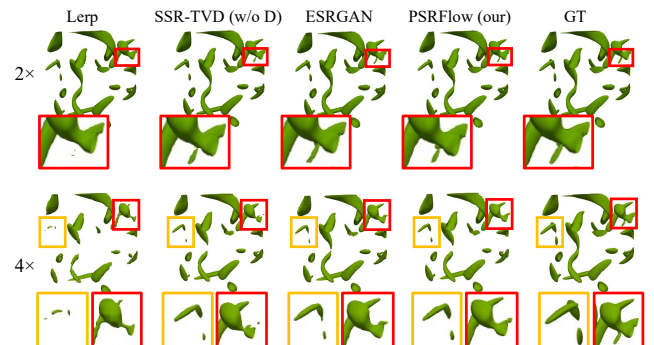

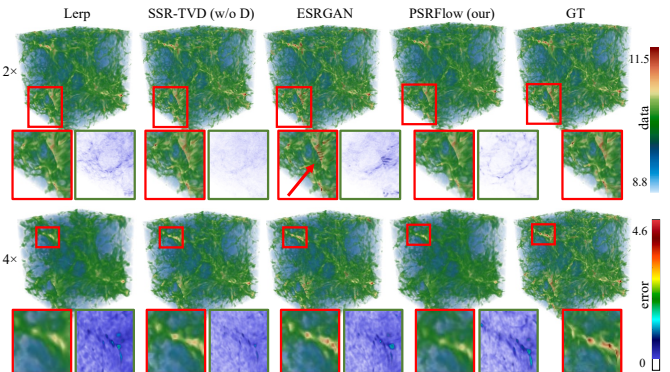Fig. 7: Isosurface rendering of baselines' and PSRFlow's super-resolution results, and ground truth for Vortex data.

Fig. 8: Volume rendering of baselines' and PSRFlow's super-resolution results, error maps (green rectangle), and ground truth for Nyx data.

resolved results. We use the same visualization setting for all rendering results of the same dataset.

In Fig. 6, we show volume rendering images of trilinear interpolation (Lerp), SSR-TVD (w/o D), ESRGAN, and PSRFlow's super-resolution results for the Vortex dataset, and compare them with the high-resolution ground truth. The upscale factors from the top row to the bottom row are 2×, 4×, and 8×. For each super-resolution result, we provide a zoom-in region (red rectangles) at the bottom of the volume rendering image, accompanied by the corresponding squared error map on its right side (green rectangles). By comparing the volume rendering images for error maps of the proposed PSRFlow with the three baselines (the first three columns), we found that the learning-based methods can produce super-resolved data with better high-frequency details, unlike the interpolation-based method which tends to produce blurry outputs. Although SSR-TVD (w/o D), ESRGAN, and PSRFlow all produce high-quality results that are visually similar, SSR-TVD (w/o D) still contains artifacts, such as generating non-existing high vorticity magnitude voxels in the center of the vortex core, as shown in the zoom-in region of the first row (2×) in the second column of Fig. 6. However, the third row (8×) shows relatively low quality of all methods, while interpolation has the worst performance. This is anticipated since at this level, most feature information is lost in the low-resolution data, making it difficult to reconstruct the original vortex core structures accurately. We do not include SSR-TVD's qualitative evaluation here since it has low quality visually with obvious artifacts. Results of SSR-TVD are presented in the supplementary material.

Figure 7 shows isosurface rendering images of trilinear interpolation,

SSR-TVD (w/o D), ESRGAN, PSRFlow's super-resolution results, and high-resolution ground truth for the Vortex data with *isovalue* = 6. The upscale factors for the first and the second row are 2× and 4×. In the predicted high-resolution isosurface rendering images, we observed that trilinear interpolation loses isosurface features easily such as the red highlighted region in the first row and the yellow highlighted region in the second row. This is likely due to the fact that the simple trilinear interpolation method can not reconstruct complex features accurately. In the red highlighted regions of the second row, we found SSR-TVD (w/o D) also has difficulties reconstructing some details and resulting in disconnected features. ESRGAN and PSRFlow have similar high-quality super-resolution results compared to the ground truth.

In Fig. 8, we compare volume rendering results of trilinear interpolation, SSR-TVD (w/o D), ESRGAN, and PSRFlow's super-resolution results for the Nyx dataset. The upscale factors for the first and the second row are 2× and 4×. It is clear that learning-based methods can
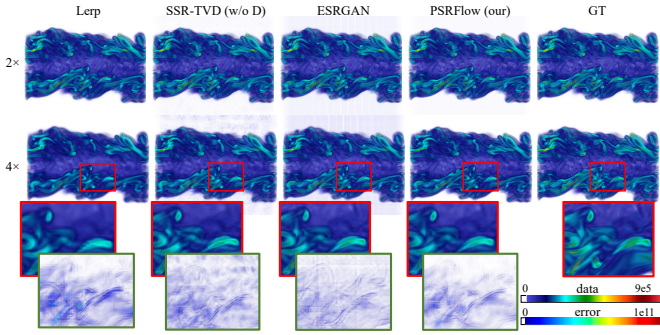
Fig. 9: Volume rendering of baselines' and PSRFlow's super-resolution results, error maps (green rectangle), and ground truth for Combustion.

produce improved details in super-resolved results than trilinear interpolation. Overall SSR-TVD (w/o D), ESRGAN, and PSRFlow produce similar high-quality results. However, ESRGAN can generate artifacts that do not exist in the original high-resolution data. For instance, in the red highlighted regions of the first row, ESRGAN (the third column, red arrow) produces non-existing high-density features. This poses a challenge for scientists to trust GAN's super-resolution outputs.

Figure 9 shows volume rendering images of baselines' and PSRFlow's super-resolution results, and error maps for Combustion data. From the zoom-in regions in the second row, we can see that deep learning based methods can produce sharper reconstructions with higher-quality features compared to interpolation-based methods. However, when compared to PSRFlow, SSR-TVD (w/o D) and ESRGAN produce noticeable artifacts in both the error maps of zoom-in regions and the background area of the whole reconstruction's rendering images.

In conclusion, SSR-TVD (w/o D), ESRGAN, and PSRFlow all can produce high-quality super-resolution results, however, since SSR-TVD (w/o D) and ESRGAN are all GAN-based models, they have training instability problems and are easy to generate artifacts. As a result, error analysis and uncertainty estimation have become crucial for scientists to gain trust to the super-resolution results. In this respect, PSRFlow outperforms all other methods with reliable uncertainty quantification. We focus on uncertainty quantification of PSRFlow in the next section.
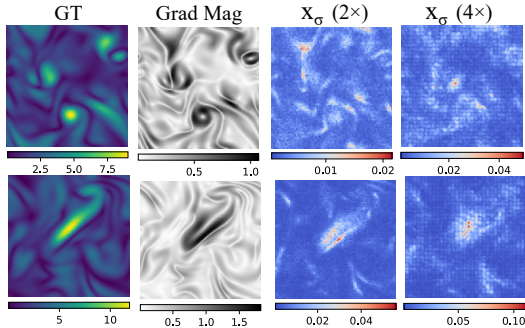

Fig. 10: Uncertainty analysis of PSRFlow's super-resolution outputs on Vortex data. Each row is a slice from the 3D data. The four columns are high-resolution ground truth (GT), its gradient magnitude (Grad Mag), and estimated uncertainties ($\mathbf{x}_\sigma$) for upscale factor $2\times$ and $4\times$.
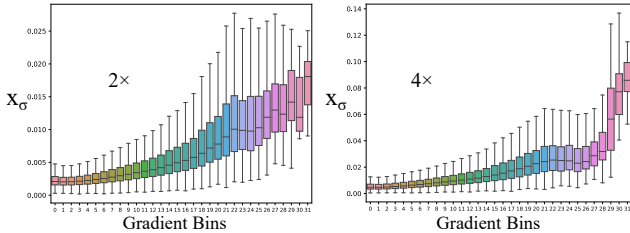

Fig. 11: Uncertainty value distribution for each gradient magnitude bin.

5.5 Uncertainty Quantification

Due to the explicit distribution modeling, PSRFlow captures the variations of missing high-frequency information in the Gaussian latent
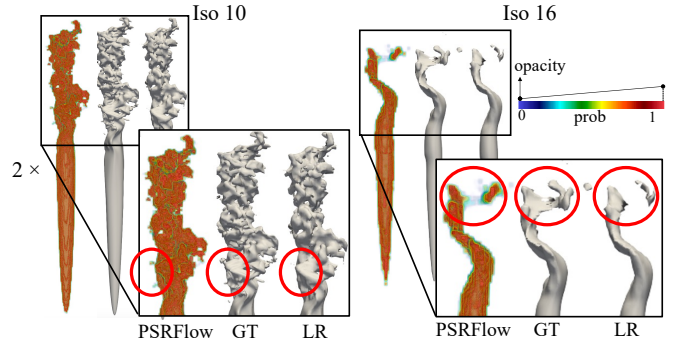

Fig. 12: Level-crossing probability visualization and isosurface rendering of Plume data with *isovalue* = 10 and 16, with a scaling factor of $2\times$.

space. Given a low-resolution input, PSRFlow allows exploring the corresponding super-resolved data space by sampling from the Gaussian latent space. Each sample will reconstruct one realization of the high-resolution data. By measuring and analyzing the variation among multiple realizations, we can estimate the uncertainties of PSRFlow's super-resolution outputs. In this section, we estimate uncertainties via Algorithm 1, where we set the number of samples $N = 40$.

5.5.1 Sources of Uncertainty

In this section, we analyze the source of uncertainty.

In Fig. 10, we show the results on the Vortex data. Each row in Fig. 10 corresponds to a 2D slice from the 3D data. The first two columns are the high-resolution ground truth and its gradient magnitude field. The next two columns are the estimated uncertainties of the high-resolution data ($\mathbf{x}_\sigma$) for upscale factor $2\times$ and $4\times$, respectively. The gradient magnitude field uses a colormap from white to black whereas regions with higher gradient magnitude will be darker. $\mathbf{x}_\sigma$ use a colormap that goes from blue to red with white in the middle. In Fig. 10, the variation in high-resolution data ($\mathbf{x}_\sigma$) reveals clear patterns of high-uncertainty regions. Comparing $\mathbf{x}_\sigma$ with the gradient magnitude field of the ground truth, we find that the high-uncertainty (high-variation) regions are likely to be regions with higher gradients. To verify this, we plot and analyze the correlation between the uncertainty values and the gradient magnitude values in Fig. 11. We compute the histogram of gradient magnitudes using 32 bins. For each bin, we calculate the mean and variance of all voxels' uncertainties in this bin and plot them as a boxplot in Fig. 11. The x-axis of each boxplot represents the gradient magnitude bins, while the y-axis represents the uncertainty values. As the gradient magnitude increases, there is a clear trend that the mean uncertainty in each bin will also increase for both upscale factors $2\times$ (left) and $4\times$ (right).

One possible reason for the correlation is that high-gradient regions tend to have more complex features than flat regions. When these regions are downsampled, the high-frequency gradient information gets smoothed out. Thus, one low-resolution input may correspond to multiple possible high-resolution outputs, and the variations occur at the complex regions (e.g., high-gradient regions). In this case, the model has lower confidence and higher uncertainties in complex regions of the super-resolution output. For simple regions, there are fewer variations and the model is more confident and less uncertain about the output.

Comparing the spatial and value distributions of the variations in high-resolution data ($\mathbf{x}_\sigma$) for different upscale factors in Fig. 10 and Fig. 11, we find that when the upscale factor is increased from $2\times$ to $4\times$, we have regions with increased uncertainties and the value range of uncertainties is also increased. This is probably because as the upscaling factor increases, the complexity of the super-resolution problem also increases, making it more challenging to estimate fine details due to the large information loss. There are more ambiguities during super-resolution, thus the level of uncertainty is increased.

Fig. 12 shows the level-crossing probabilities computed using the probabilistic marching cubes algorithm [31] for PSRFlow's output, along with isosurface rendering images of the ground truth (GT) and the low-resolution data (LR) for the Plume dataset at *isovalue* = 10
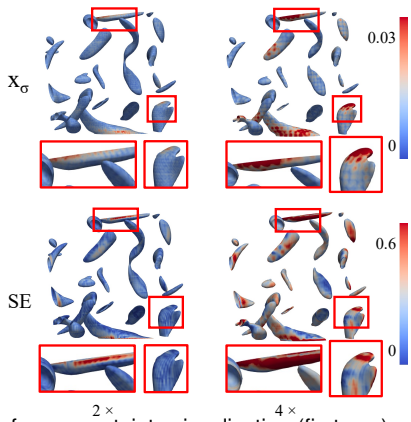
Fig. 13: Isosurface uncertainty visualization (first row) and isosurface squared error visualization (second row) of Vortex data with *isovalue* = 6.
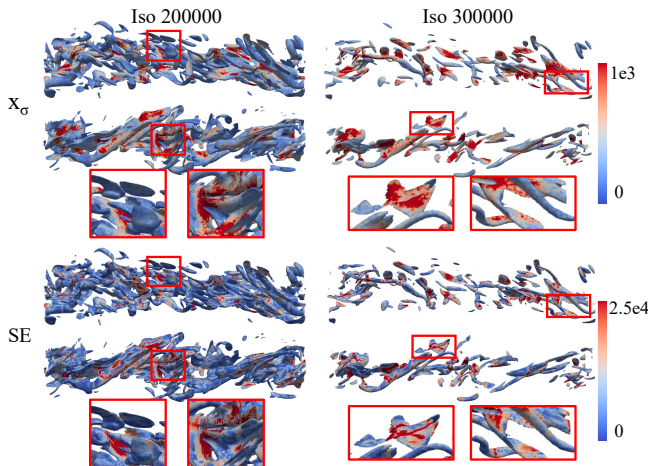

Fig. 14: Isosurface uncertainty visualization (first row) and isosurface squared error visualization (second row) of the Combustion dataset.

and 16. The upscaling factor employed is 2×. We render the level-crossing probability field of PSRFlow's super-resolution results, where red (opaque) represents the high probability, and blue (transparent) represents the low probability. By comparing the probability field with the ground truth and low-resolution data, we observe that PSRFlow is able to reconstruct missing features in the low-resolution input. However, since the low-resolution information is incomplete, the model exhibits lower probabilities in these regions, as highlighted by the red circles, which indicate higher uncertainties. This is expected since the model is given limited input information and its performance heavily depends on the quality of the low-resolution input.

In summary, the uncertainties come from the variations of possible high-resolution data. When the model is not sure about the exact super-resolved data it should produce based on the low-resolution input, it will have higher uncertainties in these high-variation regions.

5.5.2 Uncertainty for Error Analysis

In this section, we analyze the correlation between errors and uncertainties in PSRFlow's outputs on the Vortex and Combustion data.

Fig. 13 shows isosurface uncertainty and isosurface error visualization for the Vortex dataset with *isovalue* = 6. The error refers to the squared error calculated between the mean of the PSRFlow's outputs and the high-resolution ground truth. Uncertainties ($\mathbf{x}_\sigma$) and squared errors (SE) are encoded directly on the surfaces using color, with red indicating higher values. The first row shows isosurfaces uncertainties and the second row shows squared error maps. The columns are results for scaling factors of 2× and 4×, respectively. When comparing the uncertainties of 2× and 4× results, we also observe an increase in uncertainty in many regions as the upscaling factor increases. Meanwhile, our uncertainty shows blob-like artifacts, this is due to the sampling in the latent space. As the latent space provides a wider receptive field,

instead of pixel-wise uncertainty, we have blob-like patterns in uncertainty. By comparing the zoom-in regions in red rectangles across rows, we found the regions with high uncertainty also exhibit higher squared errors. This is because high-uncertainty regions are areas with high ambiguity and high variation due to the information loss, the model is less confident in these regions and errors are more likely to occur in these highly uncertain regions. This demonstrates that we can utilize uncertainty as an indication of the quality of super-resolution outputs.

Fig. 14 shows isosurface uncertainty and isosurface error visualization for the Combustion dataset. The two columns represent results for *isovalue* = 200000 and 300000, respectively. Similar to previous findings, the red rectangles in the rendering images also reveal a correlation between uncertainty ($\mathbf{x}_\sigma$) and error (SE) for each isovalue.

During post-hoc analysis, when the ground truth high-resolution data is not available, scientists cannot assess the quality of super-resolution outputs. Reliable uncertainty quantification is crucial in this case since it provides scientists with indications about what degree of confidence the scientists should have toward the super-resolution results. In the future, to improve the model's performance, one can augment the training data in these highly uncertain regions to reduce testing errors. Previous learning-based super-resolution methods, despite their high performance, lack the ability for error estimation and uncertainty quantification, which can be offered by the proposed PSRFlow.

6 DISCUSSION AND FUTURE WORK

Normalizing flow is attractive due to the effective probabilistic distribution modeling and uncertainty quantification. We have demonstrated PSRFlow can be used for spatial super-resolution with uncertainty quantification. There are still several limitations to our work.

First, the super-resolution quality is largely affected by the quality of the low-resolution data which can be improved by considering data importance during downsampling. Also, we do not guarantee temporal coherence for the super-resolved outputs. In the future, we would like to extend our approach to the temporal domain and quantify the uncertainties caused by the temporal super-resolution of features.

Second, normalizing flows have limitations such as network capacity and dimensionality constraints. So instead of invertible modeling between a complex data space and a Gaussian latent space, we can reduce the data size by encoding data into a latent space and using the flow model to learn the transformation between a complex latent space and a Gaussian latent space for efficient data generation and likelihood estimation. This also reduces the computational cost of training deep and complex normalizing flows.

Third, our goal is to add high-frequency details to the low-resolution data through stacked normalizing flow steps. However, this is still an estimation imposed by the training loss. One direction to improve is to restore the missing high-frequencies explicitly in the Fourier domain. For example, utilize normalizing flows based on wavelets.

Uncertainty quantification with normalizing flows is a promising research direction for deep-learning-based scientific visualization. In the future, we would like to use flow models to improve the reliability of neural network outputs for various scientific visualization applications.

7 CONCLUSION

In this paper, we propose PSRFlow, a novel deep learning based super-resolution algorithm with uncertainty quantification. Our work is based on normalizing flows to model the relationships between low and high-resolution data. The missing high-frequency information is captured in the Gaussian latent space. The Gaussian distribution allows efficient exploration of the high-resolution space given the low-resolution input. By sampling from the Gaussian latent space multiple times, one can compute the variations of the high-resolution data for uncertainty estimation. The quantified uncertainties can serve as indications for potential errors in the super-resolved results when the ground truth is no longer available. With cross-scale training, we can utilize one trained model recursively for flexible super-resolution of different scales. Our experimental results demonstrate that our model can achieve high-quality super-resolution and effective uncertainty quantification.

REFERENCES

[1] V. Aggarwal, M. Cotescu, N. Prateek, J. Lorenzo-Trueba, and R. Barra-Chicote. Using Vaes and Normalizing Flows for One-Shot Text-To-Speech Synthesis of Expressive Speech. In *ICASSP 2020 - 2020 IEEE International Conference on Acoustics, Speech and Signal Processing (ICASSP)*, pp. 6179–6183, 2020. doi: 10.1109/ICASSP40776.2020.9053678 2

[2] Y. An, H.-W. Shen, G. Shan, G. Li, and J. Liu. STSRNet: Deep Joint Space–Time Super-Resolution for Vector Field Visualization. *IEEE Computer Graphics and Applications*, 41(6):122–132, 2021. doi: 10.1109/MCG.2021.3097555 1, 2

[3] L. Ardizzone, J. Kruse, S. Wirkert, D. Rahner, E. W. Pellegrini, R. S. Klessen, L. Maier-Hein, C. Rother, and U. Köthe. Analyzing inverse Problems with Invertible Neural Networks. *arXiv preprint arXiv:1808.04730*, 2018. 2, 4

[4] M. Arjovsky and L. Bottou. Towards Principled Methods for Training Generative Adversarial Networks. In *International Conference on Learning Representations*, 2017. 3

[5] T. M. Athawale, C. R. Johnson, S. Sane, and D. Pugmire. Fiber Uncertainty Visualization for Bivariate Data With Parametric and Nonparametric Noise Models. *IEEE Transactions on Visualization and Computer Graphics*, 29(1):613–623, 2022. 2

[6] T. M. Athawale, B. Ma, E. Sakhaee, C. R. Johnson, and A. Entezari. Direct Volume Rendering with Nonparametric Models of Uncertainty. *IEEE Transactions on Visualization and Computer Graphics*, 27(2):1797–1807, 2020. 2

[7] T. M. Athawale, D. Maljovec, L. Yan, C. R. Johnson, V. Pascucci, and B. Wang. Uncertainty Visualization of 2D Morse Complex Ensembles using Statistical Summary Maps. *IEEE Transactions on Visualization and Computer Graphics*, 28(4):1955–1966, 2021. 2

[8] V. I. Bogachev, A. V. Kolesnikov, and K. Medvedev. Triangular Transformations of Measures. *Sbornik Mathematics*, 196:309–335, 2005. 2

[9] C. D. Correa, Y.-H. Chan, and K.-L. Ma. A Framework for Uncertainty-Aware Visual Analytics. In *2009 IEEE Symposium on Visual Analytics Science and Technology*, pp. 51–58, 2009. doi: 10.1109/VAST.2009.5332611 2

[10] L. Dinh, J. Sohl-Dickstein, and S. Bengio. Density Estimation using Real NVP. 2017. 1, 2, 3

[11] N. Fout and K.-L. Ma. Fuzzy Volume Rendering. *IEEE Transactions on Visualization and Computer Graphics*, 18(12):2335–2344, 2012. 2

[12] G. Grigoryan and P. Rheingans. Point-based Probabilistic Surfaces to Show Surface Uncertainty. *IEEE Transactions on Visualization and Computer Graphics*, 10(5):564–573, 2004. doi: 10.1109/TVCG.2004.30 2

[13] L. Guo, S. Ye, J. Han, H. Zheng, H. Gao, D. Z. Chen, J.-X. Wang, and C. Wang. SSR-VFD: Spatial Super-Resolution for Vector Field Data Analysis and Visualization. In *2020 IEEE Pacific Visualization Symposium (PacificVis)*, pp. 71–80, 2020. doi: 10.1109/PacificVis48177.2020.8737 1, 2

[14] J. Han and C. Wang. TSR-TVD: Temporal Super-Resolution for Time-Varying Data Analysis and Visualization. *IEEE Transactions on Visualization and Computer Graphics*, 26(1):205–215, 2020. doi: 10.1109/TVCG.2019.2934255 1, 2

[15] J. Han and C. Wang. SSR-TVD: Spatial Super-Resolution for Time-Varying Data Analysis and Visualization. *IEEE Transactions on Visualization and Computer Graphics*, 28(6):2445–2456, 2022. doi: 10.1109/TVCG.2020.3032123 1, 2, 6

[16] J. Han, H. Zheng, D. Z. Chen, and C. Wang. STNet: An End-to-End Generative Framework for Synthesizing Spatiotemporal Super-Resolution Volumes. *IEEE Transactions on Visualization and Computer Graphics*, 28(1):270–280, 2021. 1, 2

[17] M. Han, S. Sane, and C. R. Johnson. Exploratory Lagrangian-based Particle Tracing Using Deep Learning. *Journal of Flow Visualization and Image Processing*, 29(3), 2022. 2

[18] K. He, X. Zhang, S. Ren, and J. Sun. Deep Residual Learning for Image Recognition. In *Proceedings of the IEEE Conference on Computer Vision and Pattern Recognition (CVPR)*, June 2016. 4

[19] D. Hägele, T. Krake, and D. Weiskopf. Uncertainty-Aware Multidimensional Scaling. *IEEE Transactions on Visualization and Computer Graphics*, 29(1):23–32, 2023. doi: 10.1109/TVCG.2022.3209420 2

[20] R. Janosh. Random TikZ Collection. https://github.com/janosh/tikz, 12 2022. 2

[21] Y. Jo, S. Wug Oh, P. Vajda, and S. Joo Kim. Tackling the Ill-Posedness of Super-Resolution through Adaptive Target Generation. In *2021 IEEE/CVF Conference on Computer Vision and Pattern Recognition (CVPR)*, pp. 16231–16240, 2021. doi: 10.1109/CVPR46437.2021.01597 2

[22] Y. Jo, S. Yang, and S. J. Kim. SRFlow-DA: Super-Resolution Using Normalizing Flow with Deep Convolutional Block. In *Proceedings of the IEEE/CVF Conference on Computer Vision and Pattern Recognition*, pp. 364–372, 2021. 2

[23] D. P. Kingma and J. Ba. Adam: A Method for Stochastic Optimization. In Y. Bengio and Y. LeCun, eds., *3rd International Conference on Learning Representations, ICLR 2015, San Diego, CA, USA, May 7-9, 2015, Conference Track Proceedings*, 2015. 6

[24] D. P. Kingma and P. Dhariwal. Glow: Generative Flow with Invertible 1x1 Convolutions. *Advances in neural information processing systems*, 31, 2018. 1, 2, 3, 5

[25] J. Liang, A. Lugmayr, K. Zhang, M. Danelljan, L. Van Gool, and R. Timofte. Hierarchical Conditional Flow: A Unified Framework for Image Super-Resolution and Image Rescaling. In *Proceedings of the IEEE/CVF International Conference on Computer Vision*, pp. 4076–4085, 2021. 2

[26] L. Liu, A. P. Boone, I. T. Ruginski, L. Padilla, M. Hegarty, S. H. Creem-Regehr, W. B. Thompson, C. Yuksel, and D. H. House. Uncertainty Visualization by Representative Sampling from Prediction Ensembles. *IEEE transactions on visualization and computer graphics*, 23(9):2165–2178, 2016. 2

[27] A. Lugmayr, M. Danelljan, L. Van Gool, and R. Timofte. SRFlow: Learning the Super-Resolution Space with Normalizing Flow. In *Computer Vision–ECCV 2020: 16th European Conference, Glasgow, UK, August 23–28, 2020, Proceedings, Part V 16*, pp. 715–732. Springer, 2020. 2

[28] A. T. Pang, C. M. Wittenbrink, S. K. Lodha, et al. Approaches to Uncertainty Visualization. *The Visual Computer*, 13(8):370–390, 1997. 2

[29] J. Postels, M. Liu, R. Spezialetti, L. Van Gool, and F. Tombari. Go with the Flows: Mixtures of Normalizing Flows for Point Cloud Generation and Reconstruction. In *2021 International Conference on 3D Vision (3DV)*, pp. 1249–1258, 2021. doi: 10.1109/3DV53792.2021.00132 2

[30] K. Pothkow and H.-C. Hege. Positional Uncertainty of Isocontours: Condition Analysis and Probabilistic Measures. *IEEE Transactions on Visualization and Computer Graphics*, 17(10):1393–1406, 2010. 2

[31] K. Pöthkow, B. Weber, and H.-C. Hege. Probabilistic Marching Cubes. In *Computer Graphics Forum*, vol. 30, pp. 931–940. Wiley Online Library, 2011. 2, 5, 8

[32] D. Rezende and S. Mohamed. Variational Inference with Normalizing Flows. In *International conference on machine learning*, pp. 1530–1538. PMLR, 2015. 1, 2

[33] E. Sakhaee and A. Entezari. A Statistical Direct Volume Rendering Framework for Visualization of Uncertain Data. *IEEE Transactions on Visualization and Computer Graphics*, 23(12):2509–2520, 2017. doi: 10.1109/TVCG.2016.2637333 2

[34] S. Schlegel, N. Korn, and G. Scheuermann. On the Interpolation of Data with Normally Distributed Uncertainty for Visualization. *IEEE transactions on visualization and computer graphics*, 18(12):2305–2314,

2012. 2

[35] W. Shi, J. Caballero, F. Huszár, J. Totz, A. P. Aitken, R. Bishop, D. Rueckert, and Z. Wang. Real-time Single Image and Video Super-Resolution Using An Efficient Sub-pixel Convolutional Neural Network. In *Proceedings of the IEEE conference on computer vision and pattern recognition*, pp. 1874–1883, 2016. 6

[36] D. Vietinghoff, M. Böttinger, G. Scheuermann, and C. Heine. Visualizing Confidence Intervals for Critical Point Probabilities in 2D Scalar Field Ensembles. In *2022 IEEE Visualization and Visual Analytics (VIS)*, pp. 145–149, 2022. doi: 10.1109/VIS54862.2022.00038 2

[37] X. Wang, K. Yu, S. Wu, J. Gu, Y. Liu, C. Dong, Y. Qiao, and C. Change Loy. Esrgan: Enhanced Super-Resolution Generative Adversarial Networks. In *Proceedings of the European conference on computer vision (ECCV) workshops*, pp. 0–0, 2018. 6

[38] Z. Wang, A. C. Bovik, H. R. Sheikh, and E. P. Simoncelli. Image Quality Assessment: From Error Visibility to Structural Similarity. *IEEE transactions on image processing*, 13(4):600–612, 2004. 6

[39] S. Weiss, M. Chu, N. Thuerey, and R. Westermann. Volumetric Isosurface Rendering with Deep Learning-Based Super-Resolution. *IEEE Transactions on Visualization and Computer Graphics*, 27(6):3064–3078, 2021. doi: 10.1109/TVCG.2019.2956697 1, 2

[40] S. W. Wurster, H. Guo, H.-W. Shen, T. Peterka, and J. Xu. Deep Hierarchical Super Resolution for Scientific Data. *IEEE Transactions on Visualization and Computer Graphics*, pp. 1–14, 2022. doi: 10.1109/TVCG.2022.3214420 1

[41] Y. Xie, E. Franz, M. Chu, and N. Thuerey. tempoGAN: A Temporally Coherent, Volumetric GAN for Super-Resolution Fluid Flow. *ACM Transactions on Graphics (TOG)*, 37(4):1–15, 2018. 1, 2

[42] G. Yang, X. Huang, Z. Hao, M.-Y. Liu, S. Belongie, and B. Hariharan. PointFlow: 3D Point Cloud Generation With Continuous Normalizing Flows. In *Proceedings of the IEEE/CVF International Conference on Computer Vision (ICCV)*, October 2019. 2, 4